Construction and Building Materials 169 (2018) 612–628

Contents lists available at ScienceDirect

Construction and Building Materials

journal homepage: www.elsevier.com/locate/conbuildmat

Characterisation and strategies for mitigation of the contact surface unevenness in dry-stack masonry

Tatheer Zahra, Manicka Dhanasekar *

School of Civil Engineering and Built Environment, Queensland University of Technology, Brisbane, QLD 4000, Australia

HIGHLIGHTS

- Drystack masonry suffers from surface unevenness related stress concentration.
- Matrix based tactile surface sensors were used to quantify contact pressure.
- Micro finite element for surface unevenness was formulated and validated.
- Strategies for mitigating stress concentration examined.

ARTICLE INFO

Article history:
Received 28 August 2017
Received in revised form 23 February 2018
Accepted 1 March 2018

Keywords:
Drystack masonry
Contact surface unevenness
Matrix based tactile surface sensors (MBTSS)
Auxetic materials
Negative Poisson's ratio

ABSTRACT

Contact surface unevenness of the dry-stackable, interlocking blocks adversely affects the constructability of the drystack system. This paper presents the contact surface characteristics of these blocks and strategies for mitigating the unevenness through systematic experimental and numerical studies. First, the contact surface characteristics of the dry-stackable blocks have been examined experimentally using matrix based tactile surface sensors (MBTSS). High peak pressure locations on the contacting interfaces have been identified; these locations have remained unaffected by the level of the applied load in the experiment. A micro finite element modelling method incorporating the uneven contact surface has been formulated and the parameters calibrated using the experimental data. Two strategies for minimising the contact surface unevenness are then proposed (1) grinding of the surfaces of the blocks and (2) embedding a packing material between the surfaces. Both strategies have been analysed through the finite element model. The peak contact pressure is shown to have reduced considerably for the grinding strategy and when an auxetic fabric is used as an insert between the contacting surfaces of the blocks.

© 2018 Elsevier Ltd. All rights reserved.

1. Introduction

Masonry is, perhaps, the oldest construction material in the market. Its performance is highly dependent on the quality of the skilled labour laying the mortar joints. To reduce the costs of labour, several approaches have been trialled in recent years; laying thinner mortar joints through semi-skilled labour using hand-held tools [1–4] and eliminating the mortar layers through the use of interlocking blocks and relatively low skilled labour [5–10]. Dry-stacking also eliminates shrinkage cracking of the mortar joints typical of the mortared masonry [11].

On the negative side, the units must be manufactured with higher precision of their height and surface evenness. Projections of hard particles as random interstices on the contacting surfaces can adversely affect the constructability as these interstices could act as pivots leading to rocking, which would be safety hazard and drag on productivity at site.

The strength of the drystack hollow masonry is shown to be affected by the surface unevenness of the bed joint in [8]. Reduced stiffness and strength was observed due to the uneven interfaces in experimental investigations [8–10].

The surface unevenness (presence of random interstices) prevents the conformal contact between the contacting interfaces of the blocks. Experimental and numerical predictions of the joint closure characteristics of drystack masonry is reported in [9,12] and [13–14] respectively; however, the contact area and the contact pressure of the drystack blocks have not been examined widely. In [15] the characteristics of the dry joints have been examined through a sheet of carbon paper laid between two dry-stack blocks. They visually inspected the carbon paper impressions for inferring the distribution of the pressure. They reported that under

* Corresponding author.
E-mail address: m.dhanasekar@qut.edu.au (M. Dhanasekar).

https://doi.org/10.1016/j.conbuildmat.2018.03.002
0950-0618/© 2018 Elsevier Ltd. All rights reserved.

the compressive load, the interstices collapsed, which indicated presence of either low strength particles or poorly compacted surrounding matrix. Had the interstices been of high strength coarse aggregates surrounded by well compacted cement matrix, they would have resisted much higher stresses without collapse. In [16] carbon paper impressions are used to estimate the contact area of dry surfaces of sun dried interlocking blocks. The current literature is limited to only the contact surface area characterisation of drystack masonry as the carbon paper impression could not quantify the contact pressure distribution.

In this study, matrix based tactile surface sensors (MBTSS) were employed for the first time in masonry research to ascertain the contact pressure and contact area of the dry interfaces under uniform compressive loading. MBTSS sensors are very flexible and thin like a fabric. Early work at University of Illinois on rail – sleeper contact has shown quite consistent results (Greve et al., [17]; [29]) with no evidence of the effect of the sensor stiffness to the results. MBTSS is shown to precisely determine the contact area and the contact pressure with the progressively increasing compression normal to the interfaces. The results presented in this paper also conforms to the University of Illinois' experience with the MBTSS for contact area and contact pressure determinations. In this study the contact pressure distribution along the face shell of the hollow interlocking block was shown highly non-uniform. These results were validated in this research using a micro FE modelling technique.

The validated model was then employed to examine two strategies of mitigating the unevenness of the surfaces of the blocks, namely: (1) grinding of the blocks and (2) embedding a filler auxetic fabric material between the bed joints. Grinding requires value adding in the factory, whilst inserting packing material can slow down the construction productivity at site; although these economic parameters are acknowledged, this research was solely focussed on the effectiveness of these strategies to the reduction in the high levels of contact pressure for improved structural efficiency.

One of the drawbacks of the mortar layer in the traditional masonry is its higher lateral expansion (which subsequently induce vertical cracking in the blocks) due to their higher (relative to blocks) Poisson's ratio. With a view to avoiding lateral expansion, auxetic materials with negative Poisson's ratio (NPR) were selected as embedding materials in this research. Effectiveness of auxetic materials in civil engineering applications is emerging and improved structural behaviour has been reported in [19–21]; a finite element method of analysis of composites is presented in [18].

The mechanical properties obtained from the testing of the PU and auxetic foam in [21] were used in the FE analysis of foam/fabric embedded bi-stacked prisms. From the results of bi-stacked prisms analyses, an optimum strategy was selected.

This paper is structured as follows: Section 2 presents the experimental investigation on the surface characterisation of drystack blocks. Section 3 reports the experimental results. Sections 4 and 5 present the formulation and validation of the numerical modelling technique respectively for the uneven contact surface in the dry-stack masonry. Strategies for mitigation of uneven contact interface are presented in Section 6. FE analysis of drystack wallettes with optimal strategies are described in Section 7. Conclusions are presented in Section 8.

2. Experimental investigation of the contact surface unevenness

The contact area and the contact pressure were determined using two matrix based tactile surface sensors (MBTSS) inserted between the two symmetrically located contacting surfaces of the face shell under monotonically increasing vertical compressive load. Hollow concrete interlocking blocks supplied by the local manufacturer were used in this investigation. Half and full blocks of gross dimensions 200 mm wide × 200 mm high × 190 mm thick and 400 mm wide × 200 mm high × 190 mm thick respectively as shown in Fig. 1 were used.

Two course (bi-stacked) prisms were used in the experiments. To measure the contact area and contact pressure, MBTSS sensors were inserted between the symmetric face shells of the blocks as shown in Fig. 2. Maximum load in each test was limited to well below the ultimate load of the blocks.

The MBTSS equipment is shown in Fig. 3, which contains a handle 'data acquisition electronics', a sensor and a software. For this experiment, two sensors each of which had dimensions sufficient to cover a face shell (30 mm wide × 200 mm long) of the concrete half block were selected. The sensor model having size of 264.2 mm × 33.5 mm and resolution of 25.8 sensels/cm^2 – shown in Fig. 3 was used. This sensor could record a maximum pressure up to 100 MPa. The sensor consists of an array of sensels that record the pressure and the area of contact during the test. There were 2288 sensels in each tactile sensor used in the tests.

2.1. Calibration of the MBTSS sensors

The sensors were calibrated for different loads to reduce the chances of error in the readings before carrying out the actual tests. Calibration correlates the digital output from the sensels to engineering units of force and pressure. A multi-point calibration method for multiple loads was used for improved accuracy and the process was repeated for ensure repeatability of the data. In this process, the sensor was inserted between the blocks and the specimen was subject to axial compression under displacement control; the Instron load cell reaction was monitored and the loading was stopped when the reaction attained approximately 20 kN. The test was repeated for increased load levels of 40 kN, 60 kN and 80 kN; thus, four sets of load tests were performed on each specimen. The maximum load in the tests was kept well below the expected failure load of 200 kN. The actual maximum load read from the Instron load cell and that obtained from the MBTSS software (integral of the pressure) are shown in Table 1. It can be seen that the error was less than 1%.

2.2. Testing

The calibrated sensors were inserted between the blocks – one on each face shell of the block. The assembly was tested using a 300 kN INSTRON machine as shown in Fig. 4. The specimens were subjected to monotonically increasing compression at a loading rate of 60 kN/min. The maximum load was kept as 100 kN to

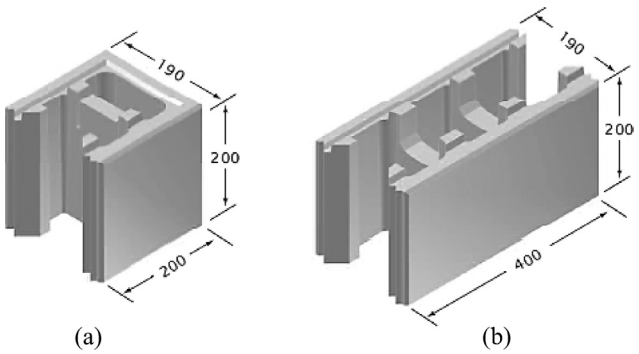

Fig. 1. Hollow concrete interlocking blocks (all dimensions are in mm). (a) Half block (b) Full block.

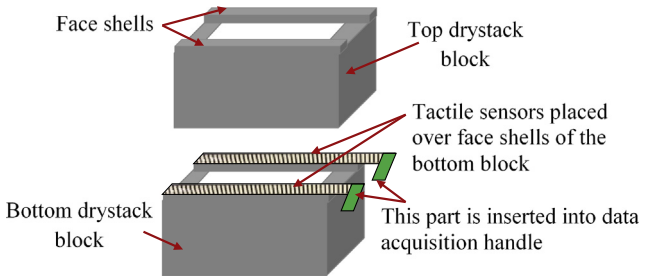

Fig. 2. Schematic representation of tactile sensors placed between the blocks.

Fig. 3. MBTSS system.

Table 1
Results of sensors calibration.

Load Increments	INSTRON (kN)	MBTSS (kN)	Difference (%)
1	20.12	20.0	0.6
2	40.15	40.25	0.3
3	60.20	59.99	0.4
4	80.27	79.95	0.4

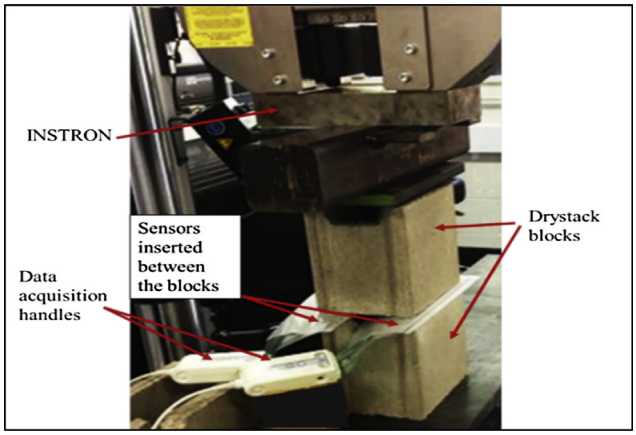

Fig. 4. Test setup for surface properties measurement.

prevent damage of MBTSS. The test was recorded using the MBTSS software [22] as a movie file. Fig. 5 shows the real time windows of the movie recording of sensors 1 and 2. Each window displayed the contact area with colour contours showing variation of contact pressure on each face shell of the drystack blocks. Four tests were performed; in each test different sets of blocks was used.

3. Experimental results and discussion

The contact area and pressure data were acquired from the recorded movie files by exporting them as ASCII data from the MBTSS software. The contact pressure contours and the contact area under the monotonic compressive loads were then plotted using the acquired data. The corresponding load data were acquired from the INSTRON machine. The applied loads, the contact pressure and the contact area from the software were synchronised based on the computer time.

3.1. Contact area

The contact area versus loading time plots for the four lab tests are shown in Fig. 6.

The total contact area was computed by adding the contact area of the two sensors (for both face shells) at each load increment. The curves have three distinct phases marked in Fig. 6:

Phase-1: The initial flat curve which showed negligible contact area during the initial loading due to unevenness of the contacting surfaces. Phase-2: With the increase in load, the contact area increased as depicted by a steeper slope. This increase shows the closing of the gaps on the contact surface under higher compressive loads. Phase-3: Maximum contact area was observed when the slope of the curves became zero which shows that the complete contact between the drystack blocks. The maximum contact area recorded was 85% to 95% of the gross area of the face shells.

The increase in contact area and the contact pressure distribution with the loading was displayed in the recorded movie during the test as depicted in Fig. 7. It can be observed that at zero load, the contact area was also null, as the load increased the contact area increased to about 50% at an applied load of 20 kN and increased to about 80% at the load of 80 kN. In addition, it was observed that the contact pressure distribution remained non-uniform over the contact surface area as shown in Fig. 7(c).

The variation of contact area with applied compressive load is shown in Fig. 8 for all the tests where maximum compressive load of 100 kN was applied.

It can be observed from the figure that at 0 kN the area is nearly zero, at 20 kN the area amplified to 5000 mm^2 (60% of the total contact area of the face shells) and at 80 kN the area increased to 7000 mm^2 (88% of the total contact area of the face shells). The data proved that the voids and interstices were collapsed when the compressive load increased leading to rapid increase in the contact area reaching the full contact (90%–95%) of the gross area was realised. Similar results have been reported in [15] who employed carbon paper to trace the contact area of the drystack blocks under increasing loads.

3.2. Contact pressure

The contact pressure distribution over the array of sensels of a single sensor (single face shell) obtained from the saved ASCII data is plotted in Fig. 9.

The pressure distribution along the face shell for the applied load of 20 kN and 100 kN is presented in 2D (Fig. 9a and b) and in 3D (Fig. 9c and d) formats. It is obvious from the pressure contours that several high pressure points exist over the contact surface and the pressure is not uniform throughout. The high pressure points persist even at higher loads which could be because of the presence of high strength coarse aggregates which did not crushed even at very high loads. The maximum contact pressure measured was 77 MPa at the highest pressure point, consistently occurring at the same pressure peak location throughout the loading along the face shell (see Fig. 9).

Fig. 10 shows the average contact pressure versus loading time relationship. The average contact pressure of the whole array of the sensels of the sensor was computed from the software. The results of the two sensors embedded in between the two face shells for all tests are shown in Fig. 10. The data from both the sensors can be

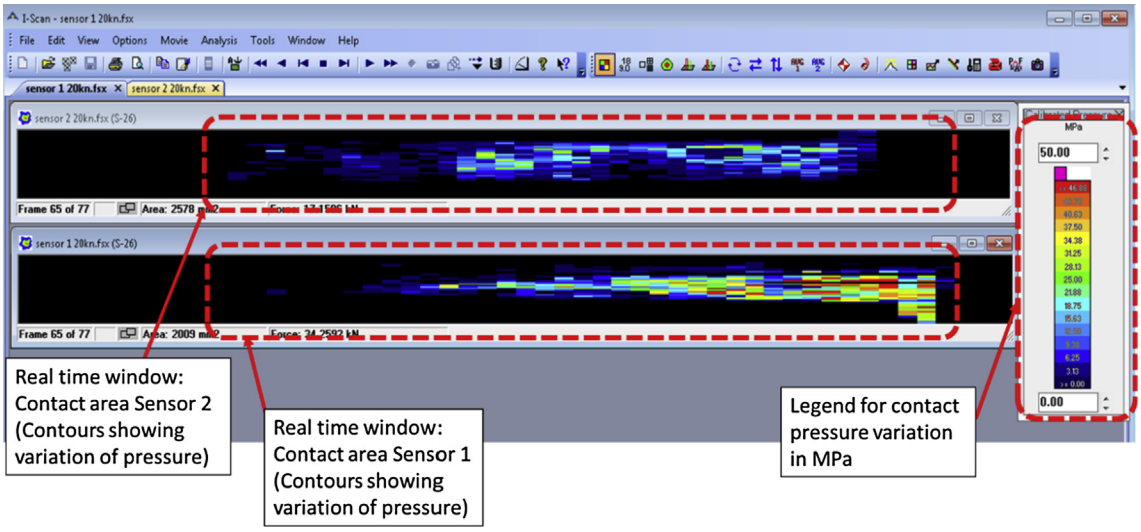

Fig. 5. Recording of the MBTSS movie during actual test.

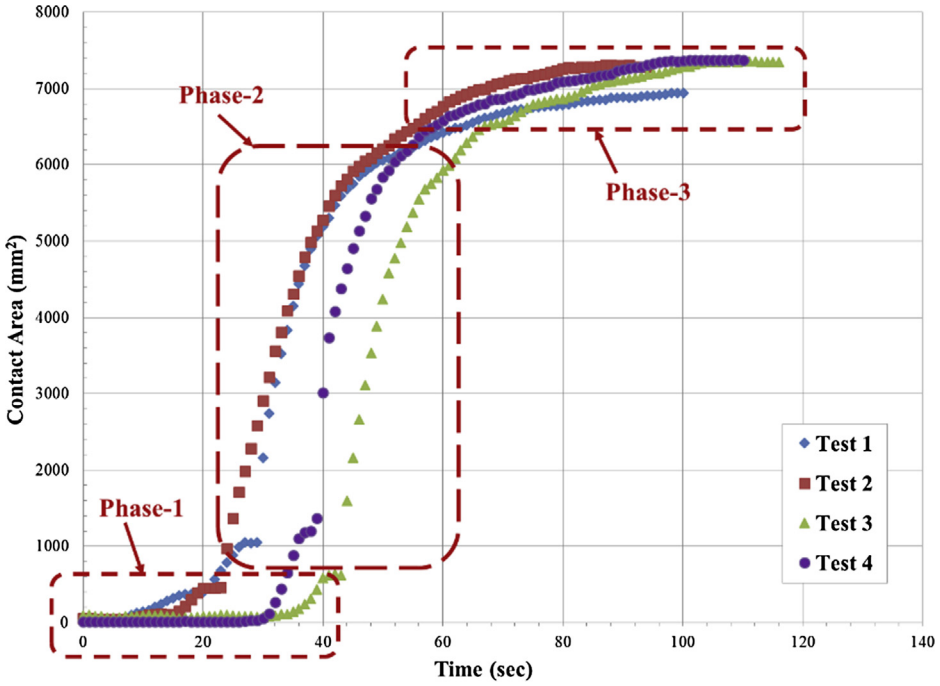

Fig. 6. Surface contact area vs. loading time using MBTSS system.

seen as consistent. The trend is similar to the contact area versus time relationship. The average contact pressure was determined as 25 MPa approximately as shown in the Fig. 10.

Fig. 11 shows the peak pressure variation with loading time from the two sensors for all tests. Although the trend is similar to the average stress, the peak stress (77 MPa) is much higher than the average values.

4. Numerical modelling technique of contact surface unevenness

To precisely model the contact surface unevenness of the drystack blocks, a micro-finite element modelling technique was formulated for the blocks shown in Fig. 12.

Only half of the specimen was modelled exploiting symmetry about z-axis as shown in Fig. 12. A three dimensional (3D) finite element modelling approach with non-linear constitutive laws for the block material and for the interface failure mechanism was used. ABAQUS finite element software was used for numerical modelling. The assembly was modelled using eight-nodded 3D elements (C3D8R). Only the face shells were uniformly loaded whilst the vertical degrees of freedom of the bottom surface were restrained as shown in Fig. 12.

4.1. Material properties

The behaviour of drystack interlocking concrete blocks was simulated using 'Concrete Damage Plasticity Model' that includes the failure mechanism of tensile cracking and compressive

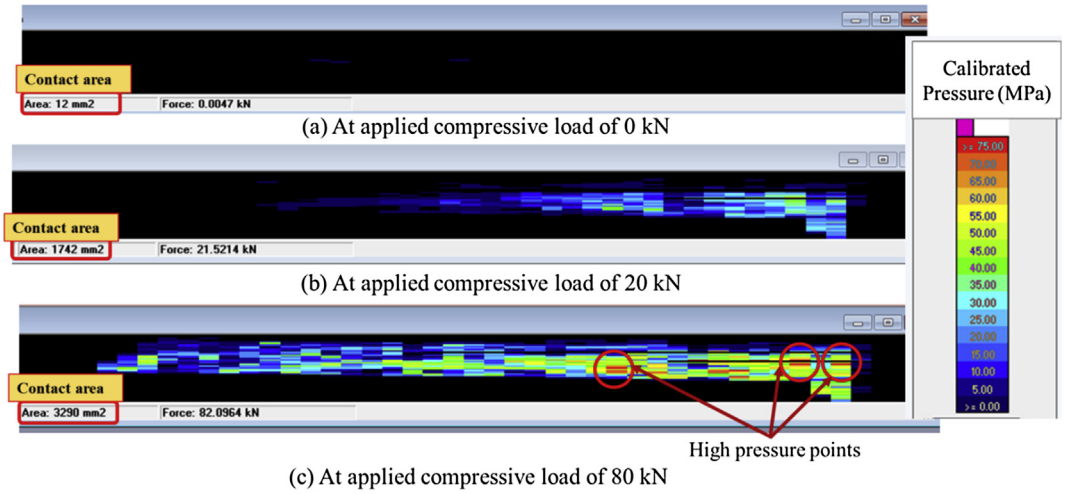

Fig. 7. Contact surface area of a single sensor for three compressive loads with pressure distribution on the contact surface.

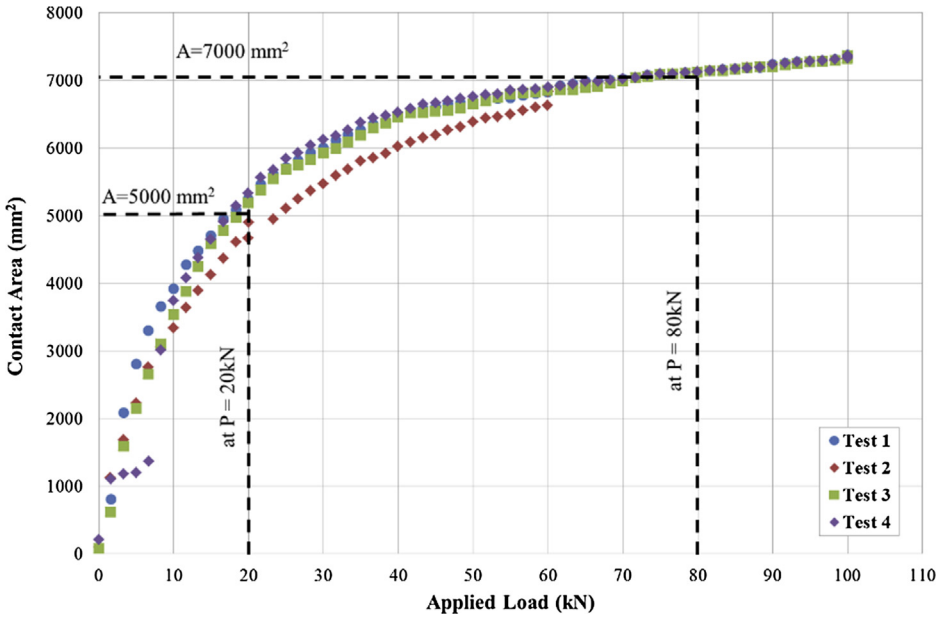

Fig. 8. Variation of contact area with increasing compressive load.

crushing. The details of material properties used for the FE model calibration are given in Table 2.

Further, the compressive and tensile failure stress-inelastic strain relations of concrete block under compression and tension were given according to Evans and Marathe [25] and ABAQUS theory manual [24]. The details are given in Table 3.

4.2. Contact surface unevenness modelling and interaction properties

To model the contact surface unevenness, two important aspects were considered (as schematised in Fig. 13):

1. Hard coarse aggregates with rock properties causing high contact pressure
2. Uneven contact surface due to the presence of interstices

A fine mesh of 2 mm in x-direction × 2 mm in z-direction × 5 mm in y-direction was used to model the peaks in a smaller area on the top of the face shell where the high pressure peaks were observed in the experiments. The properties of the meshed elements on those locations were changed to high stiff rock properties with linear elastic behaviour. The elasticity modulus and Poisson's ratio of the rock was input as 20,000 MPa and 0.25 respectively. Fig. 14 shows the model of the top face shell with uneven contact surface along with the experimental surface unevenness profile determined in Section 3.

The elements with light colour in the enlarged portion of the face shell in Fig. 14(b) show the elements representing the interstices. For the simulation of unevenness, the selected nodes were raised to 0.1 mm in the y-direction by changing the y-coordinate of the nodes. This unevenness created an initial gap of 0.1 mm between the blocks of the prism. The selection of the elements to assign the rock properties and the nodes to be elevated was carried out according to the experimental observations as shown in Fig. 14(a).

The interaction between the two interlocking drystack blocks was simulated using a constitutive law accounting for the traction-separation of the interface from the ABAQUS library. This

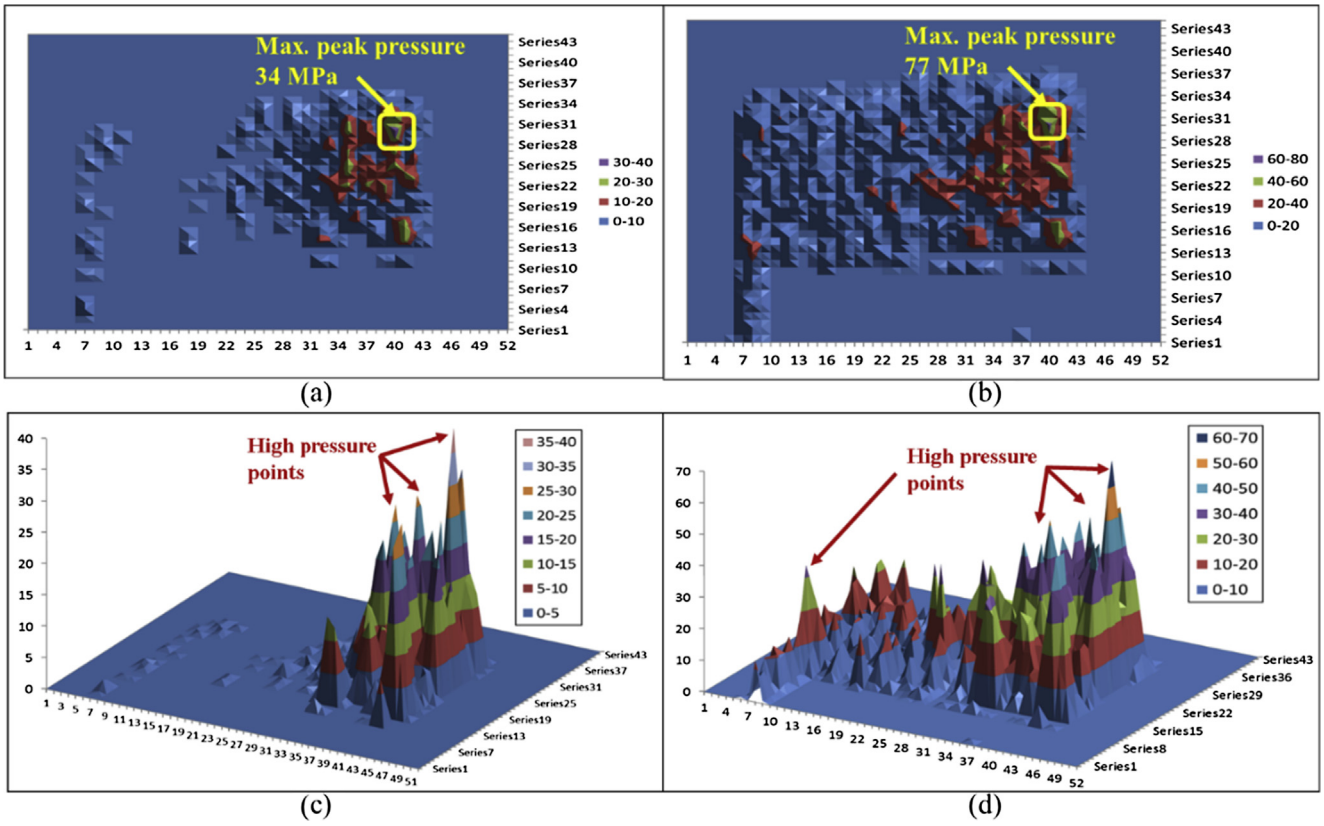

Fig. 9. Pressure distribution (in MPa) over the face shell (a) 2D at load of 20 kN (b) 2D at load of 100 kN (c) 3D at load of 20 kN (d) 3D at load of 100 kN.

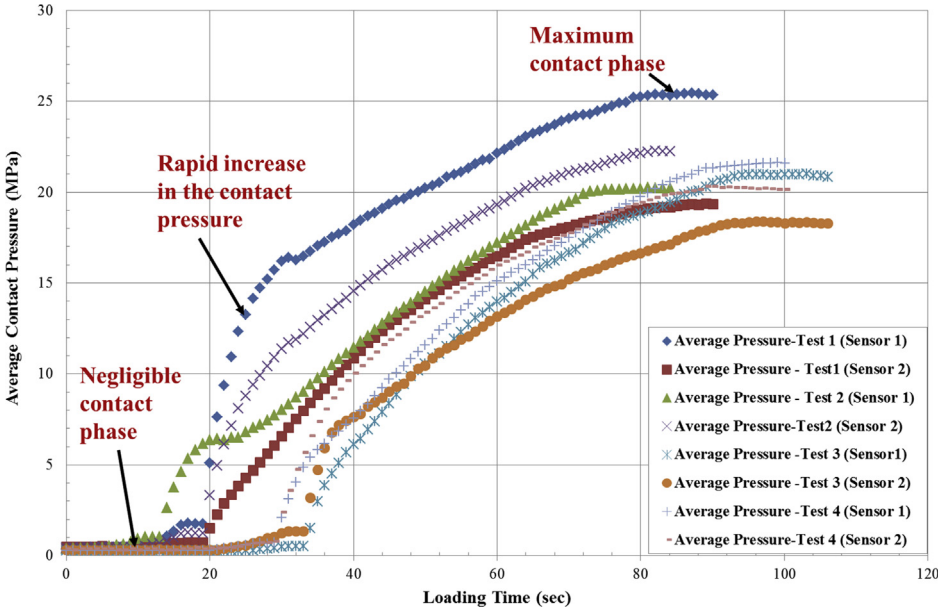

Fig. 10. Average surface contact pressure vs. loading time using MBTSS system.

model considers initially a linear elastic behaviour of the interface which is followed by the initiation and evolution of interface damage. When the interface is not in contact because of interstices, the interface behaves linear elastically. With the increase in compressive load, surface contact is established and the stresses increase until the limiting stresses are reached, after which friction model is activated which contributes to the shear stresses. Mohr-Coulomb failure criterion was used to model the friction behaviour. The selected interface properties used in the FE model are shown in Table 4.

5. Validation of the numerical model

The developed FE model of the bi-stacked drystack prisms with uneven contact surface interface shown in Fig. 15 was validated

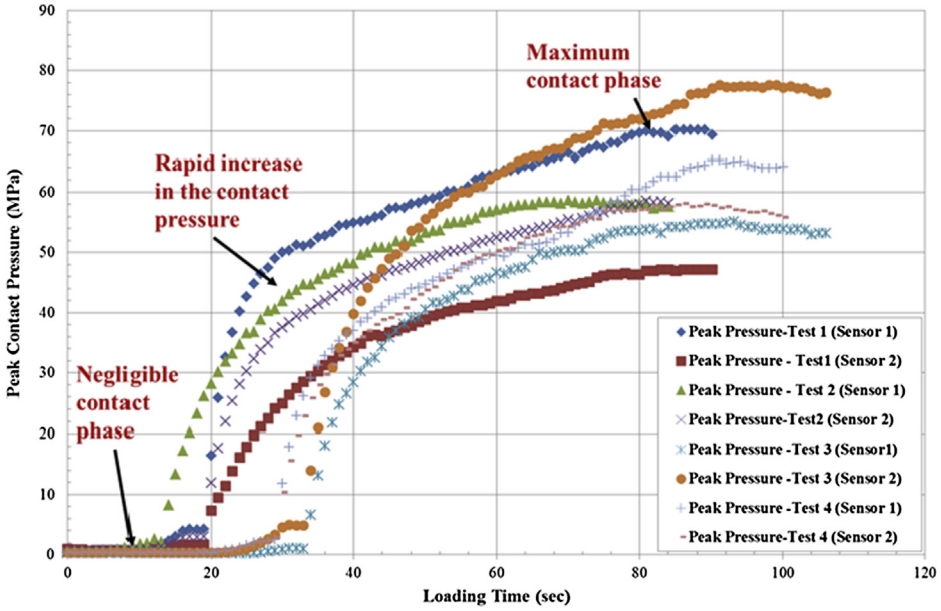

Fig. 11. Peak surface contact pressure vs. loading time using MBTSS system.

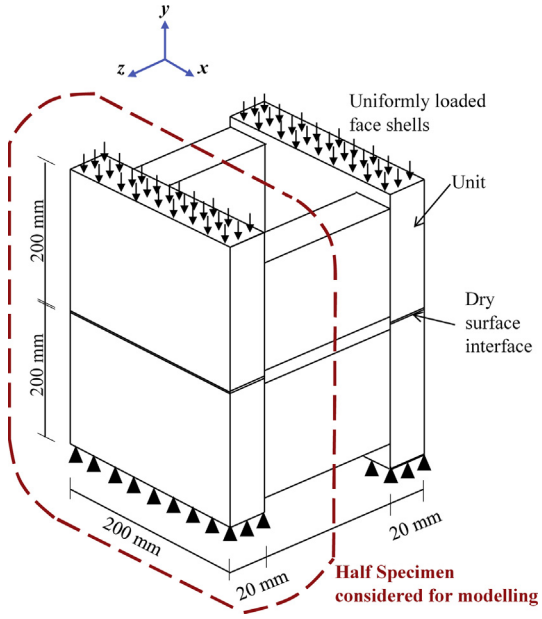

Fig. 12. Bi-stacked interlocking blocks prism assembly under compression.

Table 3
Concrete compression and tension failure stress-inelastic strain data.

Compression		Tension	
Failure stress (MPa)	Inelastic strain	Failure stress (MPa)	Inelastic strain
15	0	2.5	0
21	0.001	1.8	0.0005
25	0.002	1.2	0.0010
22	0.003	0.8	0.0015
15	0.004	0.6	0.0020
7	0.005	0.4	0.0025

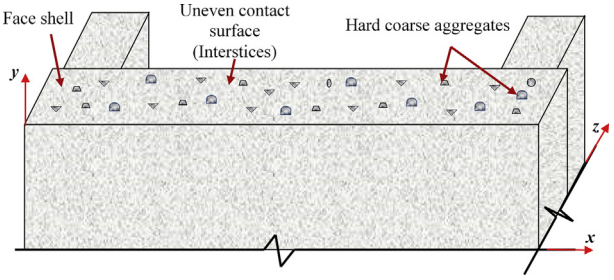

Fig. 13. Schematic representation of the surface unevenness.

Table 2
Details of concrete unit material properties used in the analysis.

Material properties	Concrete unit	References
Elastic Modulus (MPa)	9000	[23]
Poisson's ratio (υ)	0.2	[23]
Uniaxial compressive strength (MPa)	25	Manufacturer
Uniaxial tensile strength (MPa)	2.5	Assumed
Biaxial stress ratio	1.16	[24]
Dilatation angle (°)	15	[24]
Flow potential Eccentricity (ε)	0.1	[24]
Viscosity parameter	0.01	[24]

with the experimental data presented in Section 3. Since full block prisms were not tested in the lab for the contact pressure measurement due to length limitations of the MBTSS sensor, the modelling was similarly carried out for full block bi-stacked prisms. Load was applied at the rate of 60 kN/min on top of the face shell and the maximum load was kept at 100 kN to match with the experimental loading. The peak and average contact pressure curves were plotted from the ABAQUS output files.

The pressure distribution on the uneven contact surface of the half blocks was determined from the numerical model is shown in Fig. 16(b). The results of pressure distribution (pressure contours) on the surface of the contacting face shell matched well with the experimental results shown in Fig. 16(a). It can be observed from the figure that the peak pressure was 77 MPa at the same point on the face shell contact interface as was observed in the experiments.

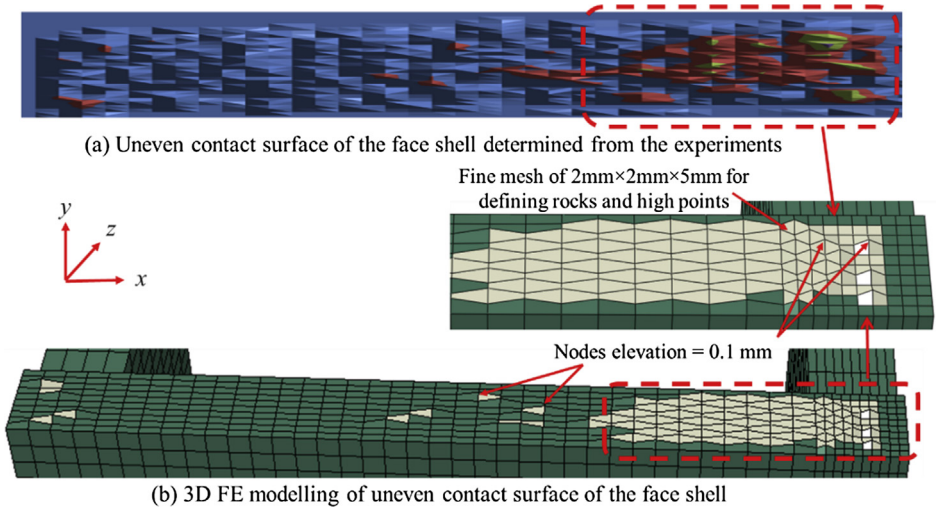

Fig. 14. Modelling of the contact surface unevenness. (Nodes elevation shown at enhanced scale).

Table 4
Interface properties.

Interface Properties	Dry interface interaction
Normal stiffness (N/mm^3)	28
Shear stiffness (N/mm^3)	32
Friction coefficient	0.6
Maximum tensile stress (MPa)	0.68
Maximum shear stress (MPa)	0.82

The variation of peak and average contact pressure with the loading time for the prisms predicted by finite element models are shown in Figs. 17 and 18 respectively.

Experimental data are also shown in these figures. Fig. 17 shows the variation of peak contact pressure with the loading time of the element as marked with the highest contact pressure in the Fig. 16. The trend obtained from the FE results compared well with that of the experimental results; the maximum peak pressure from the FE model and the lab experiments is 77 MPa. Moreover, it is notable that the results of half and full blocks are quite similar and in good agreement with the lab results. The variation of the average contact pressure computed from the FE analysis over the interface of the half and full blocks prism is presented in Fig. 18 along with the experimental data. The maximum average contact pressure from the FE model and the lab experiments are 20 MPa and 25 MPa respectively. The results computed for the full blocks are consistent with the trend observed for the half blocks.

It can be seen from the results that the stress stabilised progressively with the increase in loading showing tendency to converge towards full contact. As the load was kept elastic, well below

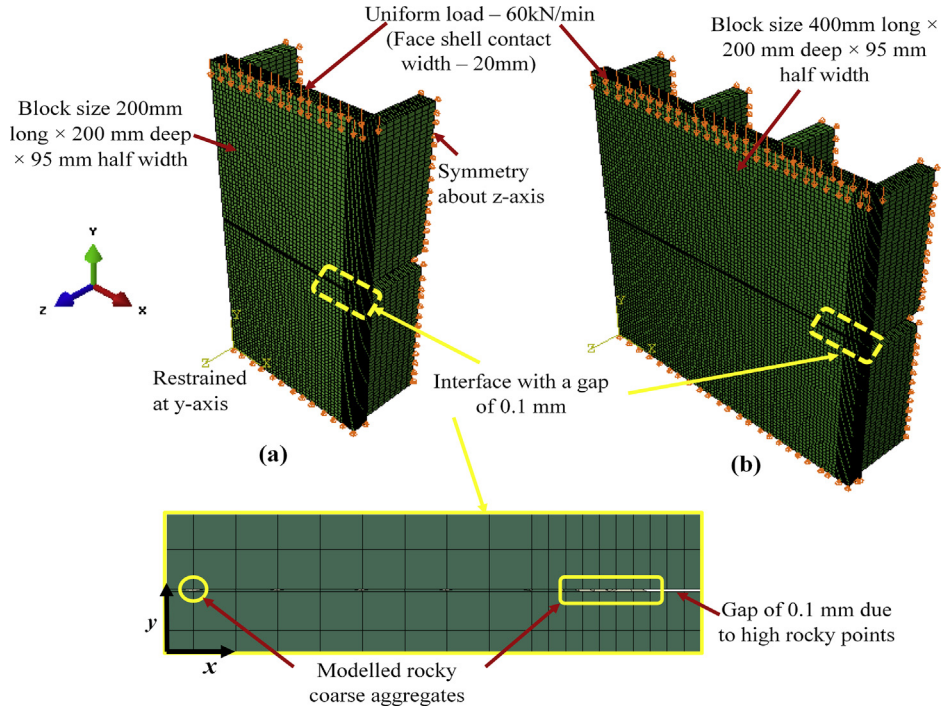

Fig. 15. FE model of bi-stacked drystack prisms with uneven contact surface. (a) Half blocks (b) Full blocks.

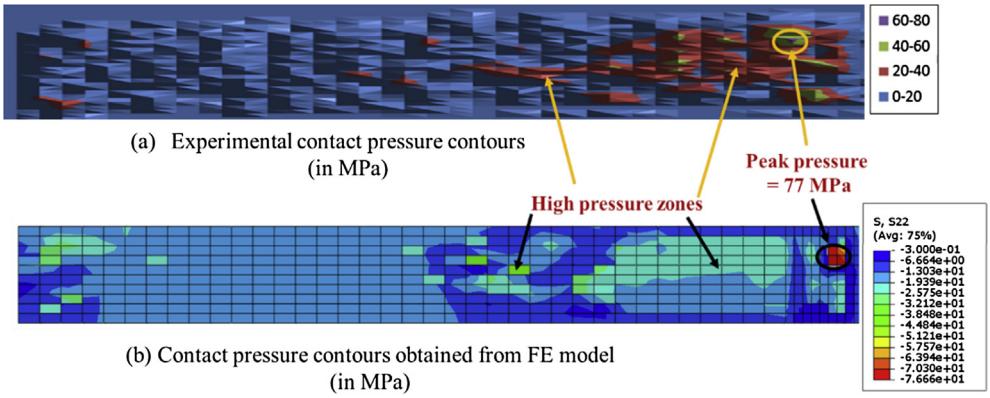

Fig. 16. Contact pressure distribution on the face shell – experimental and FE predictions.

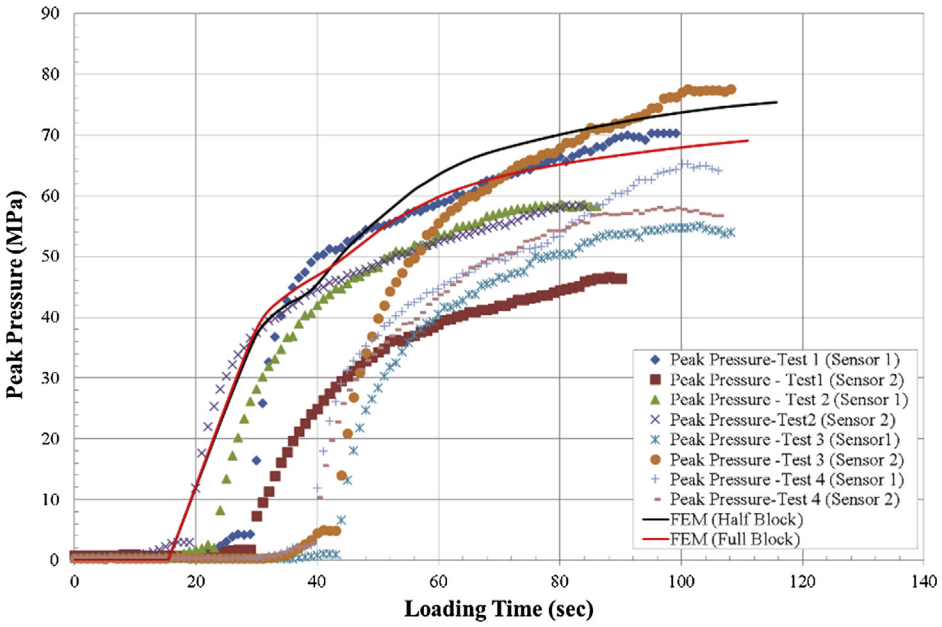

Fig. 17. Variation of peak contact pressure with loading time.

ultimate, stress-strain response from these FE analyses are not presented. With a view to demonstrating the capability of the FE model and to examine the failure modes of the drystack masonry, the FE model was later extended for wallettes analysis. Failure modes and complete load-displacement response are reported in Section 7 of this paper.

6. Strategies for mitigation of contact surface unevenness

The experimental and the numerical results presented in Sections 3 and 5 have concluded that the drystack blocks have uneven surface and hard coarse aggregates at some points creating high pressure hot-spots on the contact surface. Structurally, high pressure of magnitude 77 MPa in a unit of 25 MPa is not acceptable. Further in construction, these uneven surfaces can cause rocking of the blocks and safety hazards. Two viable strategies to mitigate this problem have, therefore, been considered:

1. Strategy-I: Grinding of the contact surface of the blocks to increase the smoothness and reducing the unevenness.
2. Strategy-II: Embedding of a material between the contacting surfaces of the blocks that can fill the gap and reduce the unevenness.

Both mitigation strategies were studied numerically using the validated contact surface micro FE model formulated in the Section 4. For strategy-I, FE analysis of bi-stacked prism with smoothly ground surface blocks has been performed under uniform compression. For strategy-II, an embedding material has been characterised through lab testing. The selected embedding materials are:

1. Polyurethane (PU) foam – commonly used as a packing foam/-filler in [21,26].
2. Auxetic foam – converted from PU foam having negative Poisson's ratio, NPR [21].
3. Auxetic Fabric – developed by an auxetic yarn of high strength and high NPR [27].

6.1. Strategy-I: FE analysis of bi-stacked prism with smoothly ground surfaces

The micro FE model presented in Section 4 was used for the analysis of the bi-stacked prism with smooth ground surfaces. The interstices were removed to obtain a smooth ground surface with no unevenness. The gap between the blocks therefore vanished. The bi-stack prism model with ground smooth surface was analysed for a uniform load of 60 kN/min on top of the face shells

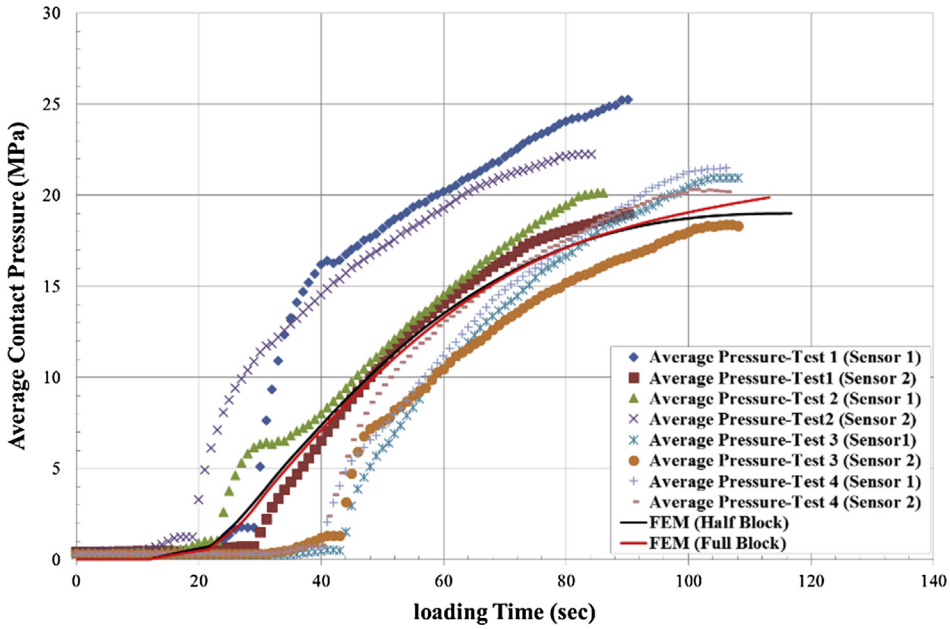

Fig. 18. Variation of average contact pressure with loading time.

which is similar to the experiments. The pressure distribution on the contact interface with the ground surface is shown in Fig. 19; for comparison, the pressure distribution with the interstices (from Fig. 16) is also shown.

It can be seen in Fig. 19 that the peak contact pressure of 77 MPa is reduced to 20 MPa at the same location where experiments showed the highest peak contact pressure. In addition, pressure distribution became uniform over the entire interface.

Fig. 20 shows the peak contact pressure versus loading time relationship. The FE results with smooth contact interface and uneven contact interface are presented. It can be observed that the peak pressure has been reduced to a low level of 20 MPa (reduced by 75%) – at the location marked in Fig. 19 due to grinding strategy. In addition, the nonlinear progressive stiffening behaviour has been eliminated due to absence of interstices. Similar behaviour was observed for the average contact pressure variation with loading time as shown in Fig. 21. The average pressure reduced from 20 MPa to 16 MPa.

The proposed mitigation strategy to grind the contact surface of the drystack blocks has thus been shown to improve the contact pressure distribution of the dry joint. However, it is difficult to perfectly grind the surface of the blocks and the process can be very expensive adding to the cost of the walls.

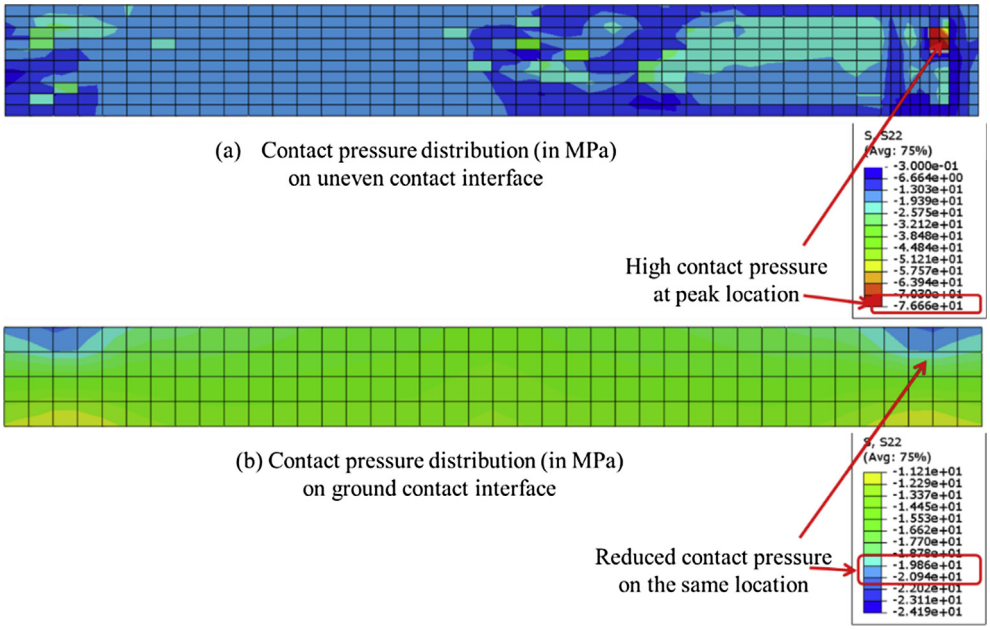

Fig. 19. Comparison of contact pressure distribution for uneven and ground interfaces.

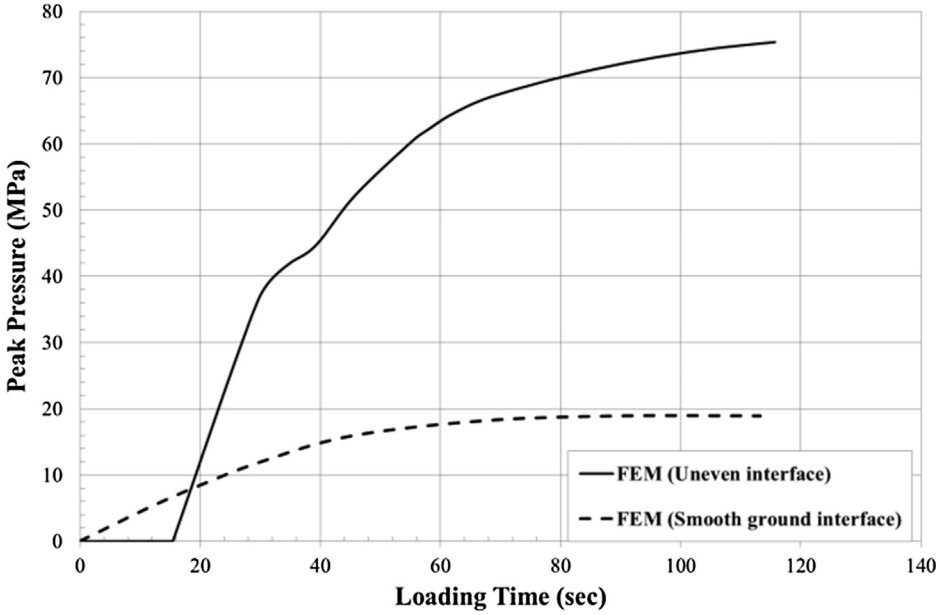

Fig. 20. Variation of peak contact pressure (at peak point) with loading time.

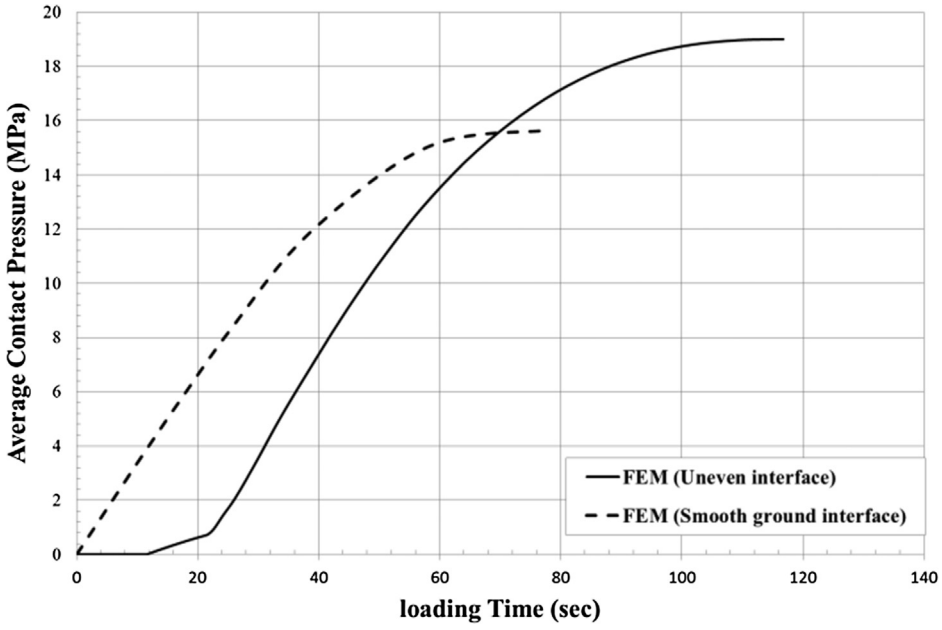

Fig. 21. Variation of average contact pressure with loading time.

6.2. Strategy-II: FE analysis of bi-stacked prisms with embedded materials

The micro FE model presented in Section 4 was used for the examination of strategy-II. Bi-stacked hollow concrete prisms with uneven contact surface riddled with interstices was considered. A layer of material was inserted between the contacting interfaces. Three types of materials (PU foam, auxetic foam and auxetic fabric) were considered. Characteristics of PU and auxetic foam can be seen in [21], the material properties were used here to examine the PU and auxetic foam embedded drystack masonry prisms. Auxetic fabric was characterised in the QUT lab (Fig. 22) for its tensile strength, Poisson's ratio and complete stress-strain curves.

6.2.1. Characterisation of auxetic fabric under tension

The auxetic fabric was manufactured with an auxetic yarn as described in [27]; the tensile strength was 50 MPa and NPR was −2.7. The fabric was cut into dumbbell shaped specimens of gauge length 60 mm × 12 mm width as shown in Fig. 22(a). The thickness of fabric was measured using a screw gauge as 1 mm. Tensile test was conducted using a 1 kN INSTRON 5566 machine; images were acquired for the digital image correlation (DIC) method [28]. Three (3) specimens, testing equipment and typical DIC mesh are shown in Fig. 22(c).

Uniform displacement of 1 mm/min was applied on the specimens. The middle of the specimens was marked to give a better texture for accurate strain measurements. The initial image was

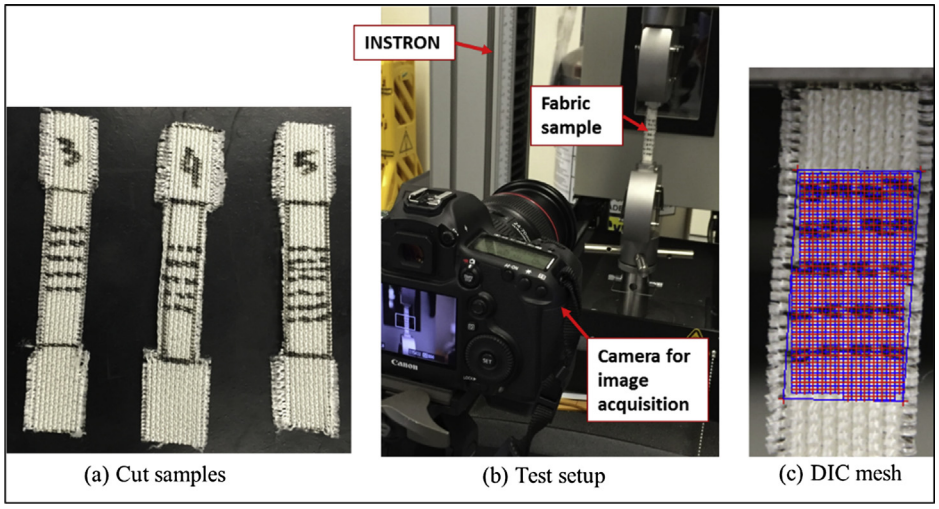

Fig. 22. Testing of auxetic fabric.

divided into a mesh of test patches (Fig. 22c). The displacement of the pixels within the patches was then used to compute the strains using DIC algorithm. The average stresses were computed using the load data acquired from the INSTRON and the gross cross section of the loaded area of the samples. The strain data from the DIC method and the stresses from the loading data were synchronised on the basis of clock time of each of the data recording computer. The stress-strain curves of the auxetic fabric specimens are shown in Fig. 23.

Three distinct phases of initial non-linear gradual stiffening phase followed by a plastic phase with permanent deformation and finally rupture can be seen from the auxetic fabric stress-strain curves presented. With the increase in the longitudinal (axial) compression, the lateral strains tended to remain constant although the axial strain monotonically increased; this phenomenon depicted gradual reduction in the NPR at higher axial strain levels. Maximum tensile strength of 50 MPa and NPR of −2.1 was observed and the stress-strain response measured from the tests is similar to as reported for the helical auxetic yarn in [27].

6.2.2. FE analysis of bi-stacked prisms with embedding materials

Prisms containing materials embedded in between the uneven contact surfaces were analysed to study the implications of embedding filler materials in drystack masonry. The material models of the PU foam, the auxetic foam and the auxetic fabric were calibrated using the experimental data. The material properties were simulated using the HYPERFOAM model available in the ABAQUS library.

Uniaxial compression test data in Table 5 was used for modelling of PU and auxetic foam. The auxetic fabric was also modelled using the same material model with the input test data presented in Table 6.

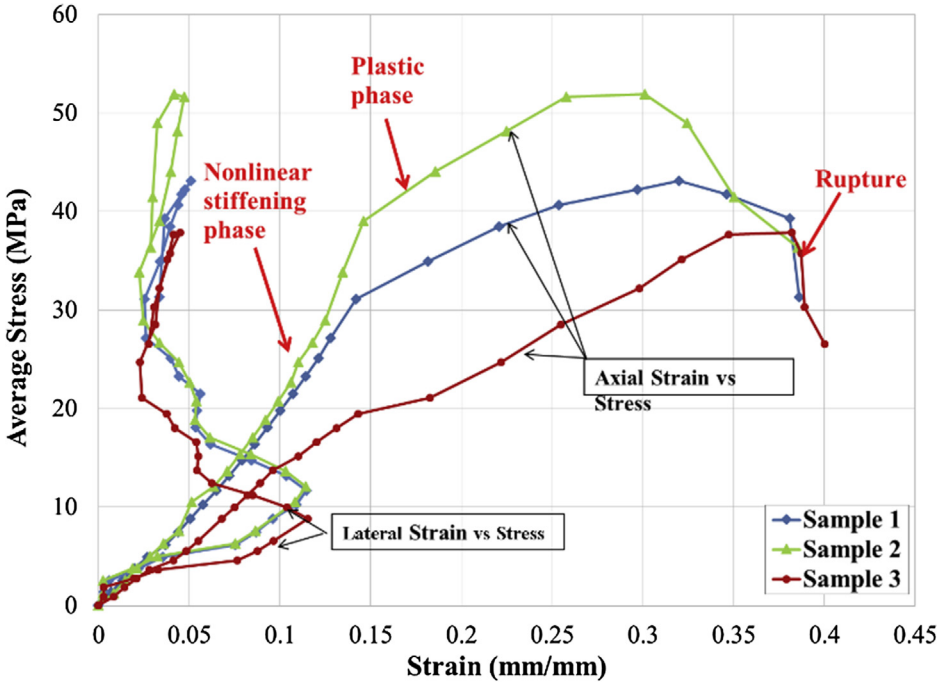

Fig. 23. Stress-strain behaviour of auxetic fabric.

Table 5
Test data used in HYPERFOAM model.

Nominal Stress (MPa)	Nominal Strain	Nominal Lateral Strain
Uniaxial compression test data of PU Foam		
0	0	0
−0.001	−0.051	0.025
−0.002	−0.106	0.050
−0.003	−0.202	0.073
−0.004	−0.297	0.094
−0.005	−0.414	0.125
−0.007	−0.508	0.088
−0.012	−0.588	0.040
−0.025	−0.700	0
−0.064	−0.800	−0.002
Uniaxial compression test data of Auxetic Foam		
0	0	0
−0.001	−0.064	−0.064
−0.003	−0.136	−0.136
−0.006	−0.250	−0.250
−0.012	−0.400	−0.400
−0.022	−0.524	−0.400
−0.042	−0.640	−0.400
−0.097	−0.800	−0.001

Table 6
Uniaxial tension test data of Auxetic Fabric.

Nominal Stress (MPa)	Nominal Strain	Nominal Lateral Strain
0	0	0
1.36	0.007	0.0027
2.58	0.013	0.0056
3.75	0.020	0.0195
4.93	0.027	0.0264
6.17	0.037	0.0363
7.46	0.044	0.0433
8.81	0.051	0.0501
10.22	0.057	0.0569
11.68	0.065	0.0643
13.19	0.072	0.0713
14.76	0.079	0.0783
21.52	0.107	0.0642
23.28	0.114	0.0396
25.13	0.121	0.0398
27.15	0.128	0.0407
31.12	0.142	0.0415
34.93	0.181	0.0515
38.48	0.221	0.0534
40.64	0.253	0.0563
42.26	0.297	0.0575
43.11	0.320	0.0582

6.2.3. Numerical results

The calibrated models for the materials embedded within the contacting interfaces were used in the 3D FE analysis of bi-stacked half concrete blocks prism. The embedding layers used are:

1. PU foam layer – 2 mm thick
2. Auxetic foam layer – 2 mm thick
3. Auxetic fabric layer – 1 mm thick

It was difficult to slice the foam less than 2 mm thick and hence 1 mm thick foams (PU and auxetic) were not trialled. The geometry, loading, boundary conditions and meshing of the materials embedded bi-stacked prisms are shown in Fig. 24. The interface properties were kept unchanged as shown previously in Table 4.

The results are shown in Fig. 25.

It was observed that the contact pressure reduced due to the embedded materials. The peak pressure reduced from 77 MPa to about 60 MPa (25% reduction) for both the PU foam and the auxetic foam embedment between the blocks. The reduction was observed higher for the auxetic fabric with a peak pressure of 40 MPa (50% reduction). In addition, the stresses were observed to have more uniform distribution when the auxetic fabric was placed in between the bed joints.

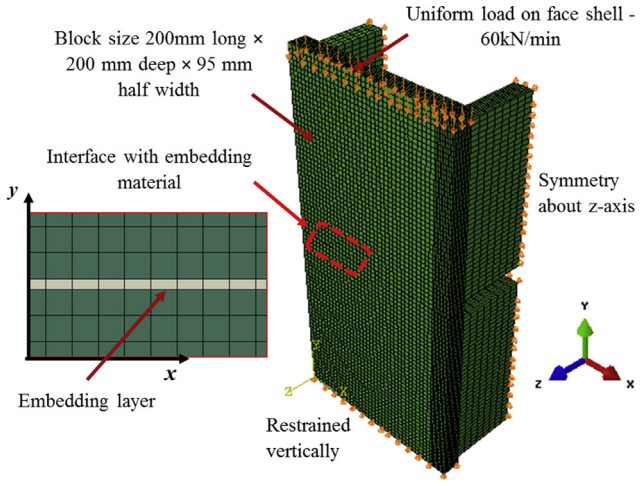

Fig. 24. FE model of bi-stacked prism with embedding material.

The variation of the peak and the average contact pressures with the loading time is plotted in Figs. 26 and 27 respectively. From both the figures, it can be observed that despite decreasing the peak contact pressure on the contact surface, the nonlinear progressive stiffening response of the joints was prolonged with PU and auxetic foam layers. The high compressibility with low compressive strength of the PU and the auxetic foam is the main cause of this behaviour. On the other hand, the auxetic fabric embedment not only reduce the peak pressure but also virtually eliminated the nonlinear progressive stiffening behaviour of the contact interfaces. Thus, it can be concluded that the 'Auxetic fabric' can be a viable solution to reduce the surface unevenness and the associated peak pressure hot-spots in the drystack masonry.

7. FE analysis of drystack wallettes with optimal mitigation

Grinding of the blocks surface and embedding the auxetic fabric in the bed joints were determined as the two strategies which can offer structural benefits through bi-stacked prisms analyses. A taller wallette was considered in this section. Wallettes of size 600 mm length × 190 mm thickness × 1600 mm height as shown in Fig. 28 were analysed. Due to symmetry along x, y and z-axis under the concentric compression load, one quarter of the wallette was modelled to economise the modelling and computational time as marked in Fig. 28. The block properties, interaction properties, meshing and element type were kept the same as detailed in Section 4. Three kinds of models were examined to ascertain the behaviour under uniform axial compressive loads:

(i) Drystack wallette with uneven contact surfaces (Wall A – base case)
(ii) Drystack wallette with smooth contact surfaces (Wall B)
(iii) Drystack wallettes with uneven contact surfaces and 1 mm thick auxetic fabric layer in between the bed joints (Wall C)

The stress distributions, the failure modes and the average stress-strain response of the wallettes were examined.

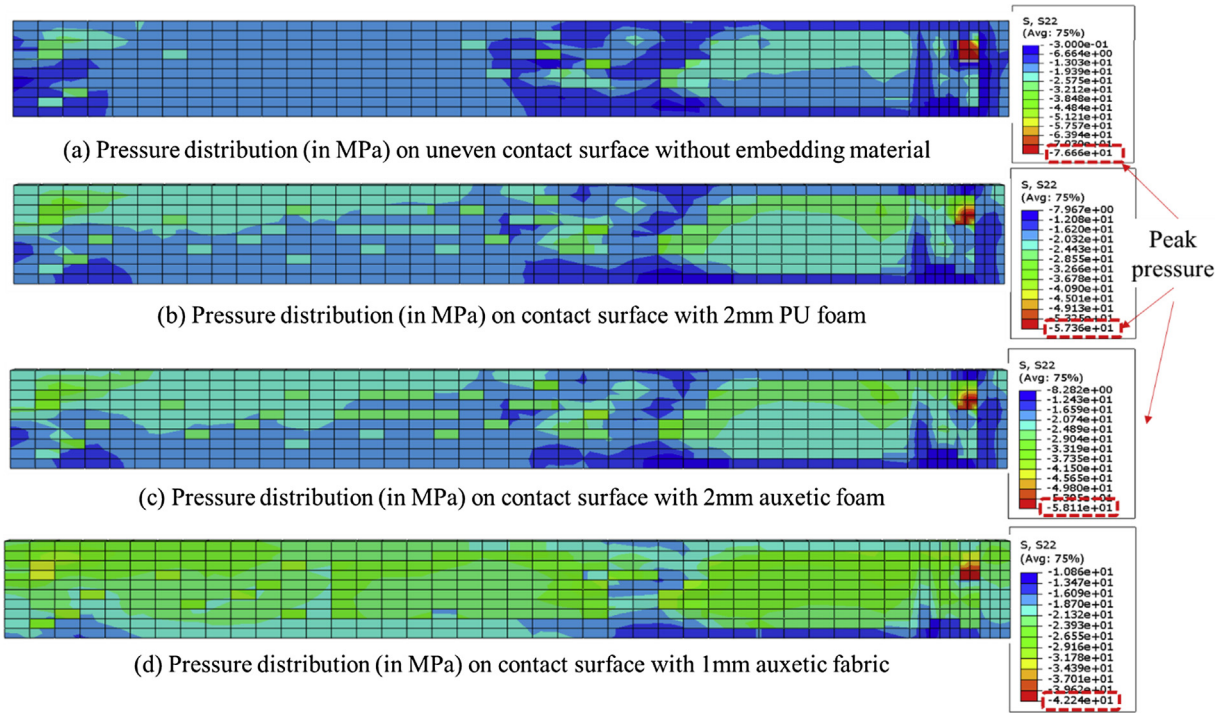

Fig. 25. Pressure distribution over contact surface with and without embedding materials.

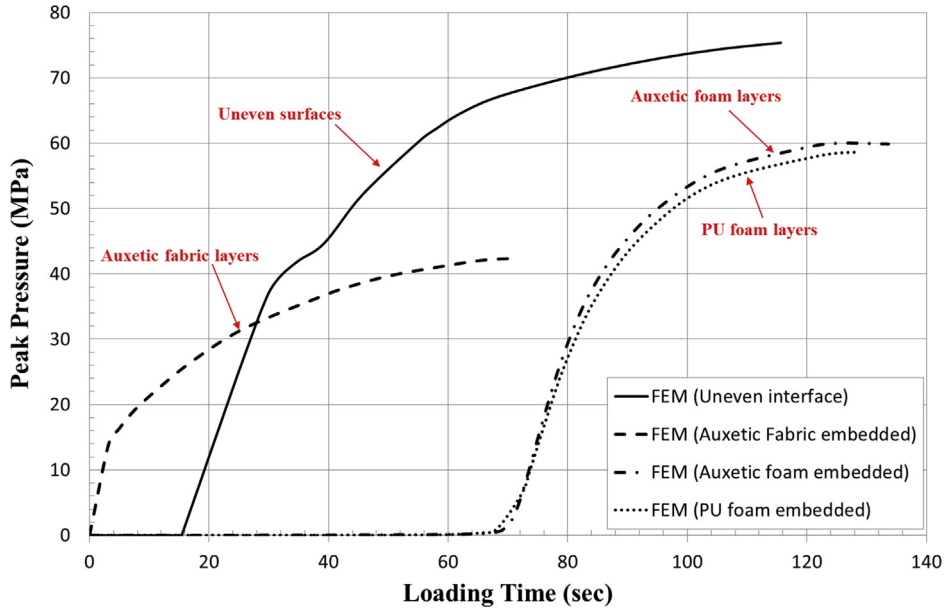

Fig. 26. Peak contact pressure with loading time.

7.1. Geometry and boundary conditions

The FE model of the wallettes with loading and boundary conditions is shown in Fig. 29.

Uniform displacement of 2 mm was applied on top of the face shells in order to understand the post peak response and the failure mechanism (not examined in the experiments). The behaviour of the auxetic fabric was simulated in accordance with the calibrated model detailed in Section 6. The interaction property between the units and between units and auxetic fabric layers was defined as previously detailed in Section 4.

7.2. FE predictions

Fig. 30 shows the vertical stress distribution in the three FE wallette models (Wall A, B and C).

The wallette with uneven contact surface (base case – Wall A) shows the excessive settlement of the joints and crushing at the ultimate stage as shown in Fig. 30(a). The wallette with the smooth ground contact surface (Wall B) experienced lower vertical stresses and minor joint deformation (crushing) as shown in Fig. 30(b). However, the drystack wallette with auxetic fabric layers (Wall C) shown in Fig. 30(c) exhibited a different behaviour of

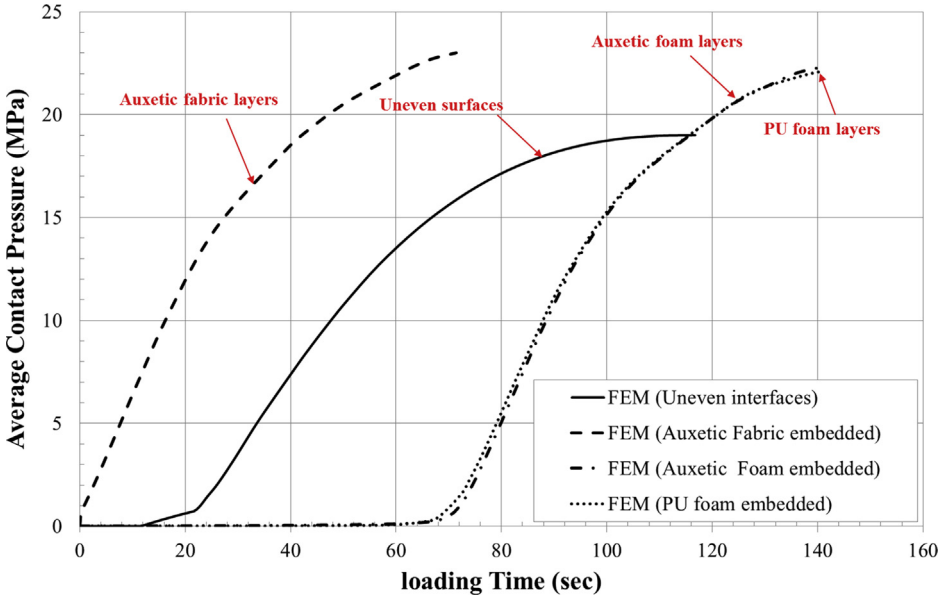

Fig. 27. Average contact pressure with loading time.

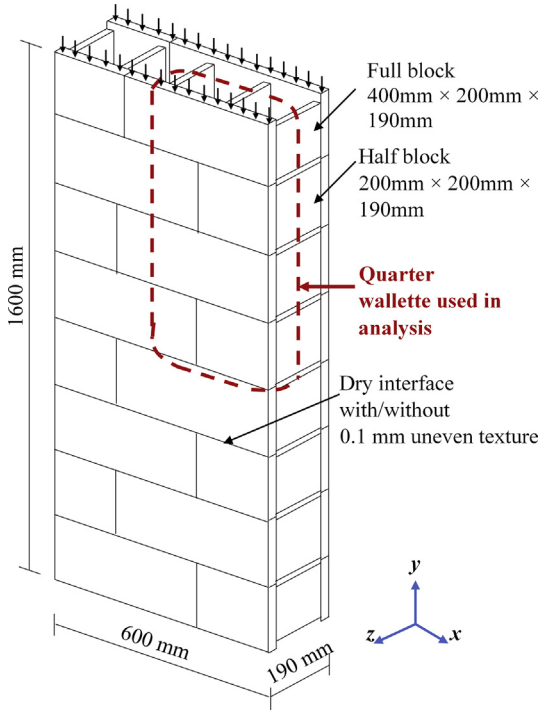

Fig. 28. Geometry of drystack wallette.

joints without any crushing of the interface. In addition, the maximum stress of 77 MPa due to interstices in the uneven surface of Wall A shown in Fig. 30(a) reduced to 42 MPa when auxetic fabric was placed in between the bed joints in Wall C as shown in Fig. 30 (c). The overall stresses decreased in the drystack wallette with even surfaces and with the auxetic fabric placed in the uneven contact interfaces. The complete (including post-peak) load – displacement response of the wallettes is shown in Fig. 31. The FE models encountered convergence problem when the peak load dropped approximately by 10% in each case.

The base case (Wall A) with uneven contact surfaces exhibited nonlinear stiffening due to gaps in between the joints. In comparison, the behaviour of the wallettes with ground surfaces (Wall B) and that with uneven contact surfaces and auxetic fabric embedded in between the bed joints (Wall C) showed improved behaviour without any nonlinear progressive stiffening. This figure shows that the large joint settlement (nonlinear progressive stiffening of the uneven joints – base case Wall "A" in Fig. 31) was completely eliminated using the two mitigation strategies (ground surfaces and embedding auxetic fabric) due to elimination of the interstices and the associated peak stresses. This improvement will, therefore, protect the walls from the brittle failure in the vicinity of joints and instability of the stacked blocks during construction.

It is anticipated that the mitigation strategies are advantageous to construction and structural response (refer to Fig. 31):

- Displacement at peak load reduced from 3.5 mm to 2.7 mm with the auxetic fabric (a reduction of 23%)
- Failure load approximately increased by 8% for auxetic inserted masonry
- The large displacement suffered by the masonry at very low load level totally vanished with the two mitigation strategies. A close look at the auxetic inserted masonry response can reveal that the auxetic fabric fully eliminate any deformation (vertical) for small loading (typically during construction). This will greatly assist the labour and improve construction productivity, which can potentially reduce cost and improve housing affordability.

Thus, it can be concluded that the placement of auxetic fabric layers in between the bed joints not only decreases the joint settlement but also increases the compressive strength of the drystack masonry.

8. Conclusions

The pressure distribution on the contacting interface area between the hollow concrete masonry blocks were determined using matrix based tactile surface sensor (MBTSS). The results were in good agreement with the available literature where carbon paper was employed for computing the contact area of the interface under increasing load. A micro FE model was formulated

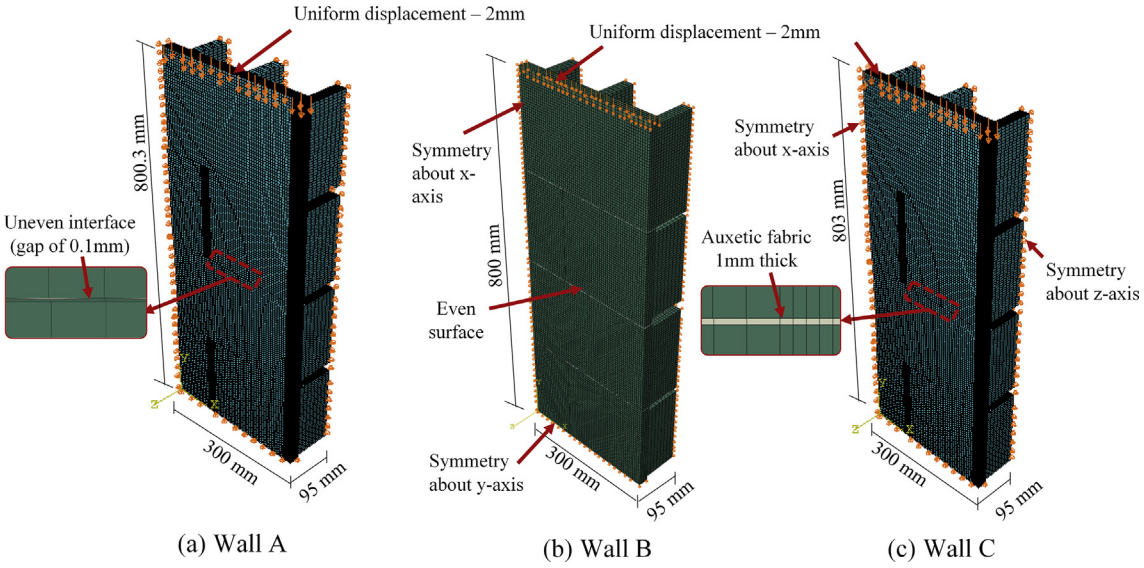

Fig. 29. FE model of drystack wallette (with and without auxetic fabric).

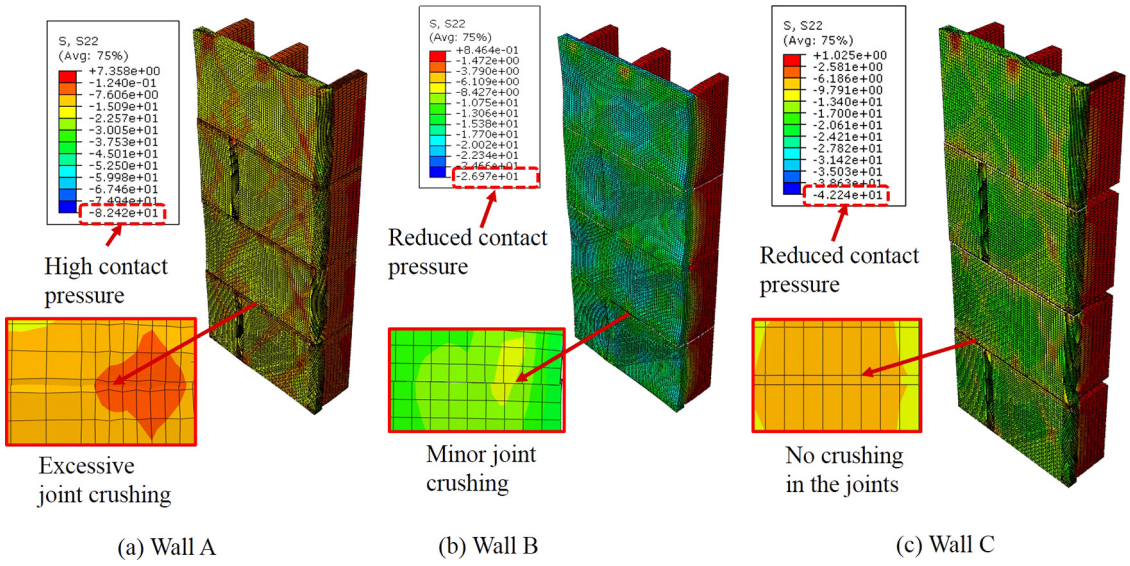

Fig. 30. Vertical stress distribution in the wallettes.

and validated using the experimental results. The results of micro FE model were also matched well with the experiments. The peak pressure and the pressure distribution over the interface was similar to that was obtained from the experiments. This implies that MBTSS can reliably be used to ascertain the contact surface properties of the drystack blocks. Two mitigation strategies of grinding the blocks surface and embedding a filler material to reduce the contact surface unevenness of the drystack blocks were investigated using a micro FE model in this research. The conclusions drawn from this study are:

- The MBTSS determined that the blocks had only about 5%–10% contact under the self-weight and approximately 95% contact at 75% of ultimate load.
- The peak pressure along the surface of face the shells was measured as three times more than the average strength of blocks due to the presence of the interstices. The contact pressure distribution was highly non-uniform along the face shell of the hollow concrete blocks.
- FE micro model was used to simulate the unevenness of the dry contact interface by raising the elevation of the nodal coordinate and assigning rock properties to the peaks on the face shell. The obtained FE results validated the experimental contact pressure adequately.
- Grinding of the surfaces and embedment of auxetic fabric between the bed joints of the drystack blocks were beneficial in reducing the peak contact pressure. Since grinding could be challenging and expensive, auxetic fabric placed between the

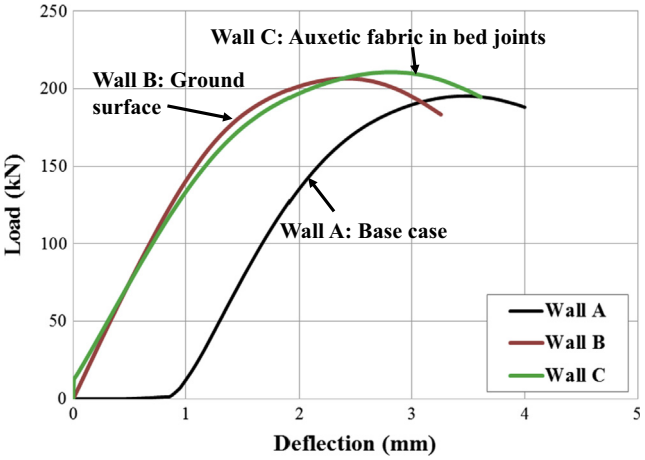

Wall	Peak Load (kN)	Deflection at peak (mm)
A	195	3.5
B	206	2.5
C	211	2.7

Fig. 31. Load – Displacement curves of drystack wallettes.

dry joints was trialled and was shown that the peak stress could be reduced by 50%.

The authors have proposed to conduct experiments on wallettes with auxetic layers in between the bed joints to extend this work in future.

Acknowledgements

The authors would like to acknowledge Queensland University of Technology, Australia for providing the Postgraduate Research Award (QUTPRA) doctoral scholarship for conducting this research. The Concrete Masonry Association of Australia (CMAA) donated the concrete blocks.

References

[1] J.A. Thamboo, M. Dhanasekar, C. Yan, Flexural and shear bond characteristics of thin layer polymer cement mortared concrete masonry, Constr. Build. Mater. 46 (2013) 104–113.
[2] S. Nazir, M. Dhanasekar, Modelling the failure of thin layered mortar joints in masonry, Eng. Struct. 49 (2013) 615–627.
[3] J.A. Thamboo, M. Dhanasekar, Characterisation of thin layer polymer cement mortared concrete masonry bond, Constr. Build. Mater. 82 (2015) 71–80.
[4] S. Nazir, M. Dhanasekar, A non-linear interface element model for thin layer high adhesive mortared masonry, Comput. Struct. 144 (2014) 23–39.
[5] K.B. Anand, K. Ramamurthy, Development and performance evaluation of interlocking-block masonry, J. Archit. Eng. 6 (2) (2000) 45–50.
[6] K.B. Anand, K. Ramamurthy, Laboratory-based productivity study on alternative masonry systems, J. Constr. Eng. Manage. (ASCE) 129 (2003) 237–242.
[7] W.A. Thanoon, M.S. Jaafar, M.R. Abdulkadir, A.A.A. Ali, D.N. Trikha, A.M.S. Najm, Development of an innovative interlocking load bearing hollow block system in Malaysia, Constr. Build. Mater. 18 (2004) 445–454.
[8] K.H. Oh, H.G. Harris, A.A. Hamid, Behaviour of interlocking mortarless masonry under compressive loads. in: Proceedings of Seventh Canadian Masonry Symposium, Ontario, Canada. June 1995 (1995).
[9] M.S. Jaafar, A.H. Alwathaf, W.A. Thanoon, J. Noorzaei, M.R. Abdulkadir, Behaviour of interlocking mortarless block masonry, Proc. Inst. Civ. Eng. Constr. Mater 159 (CM3) (2006) 111–117.
[10] K.B. Anand, K. Ramamurthy, Development and performance evaluation of hollow concrete interlocking block masonry system, TMS J. (2005) 11–20.
[11] C. Beall, New masonry products and materials, Prog. Struct. Mat. Eng. 2 (2000) 296–303.
[12] K. Andreev, S. Sinnema, A. Rekik, S. Allaoui, E. Blond, A. Gasser, Compressive behaviour of dry joints in refractory ceramic masonry, Constr. Build. Mater. 34 (2012) (2012) 402–408.
[13] T. Zahra, M. Dhanasekar, A generalised damage model for masonry under compression, Int. J. Damage Mech. 25 (5) (2016) 629–660.
[14] T. Zahra, M. Dhanasekar, Prediction of masonry compressive behaviour using a damage mechanics inspired modelling method, Constr. Build. Mater. 109 (2016) 128–138.
[15] G. Marzahn, G. Konig, Experimental investigation of long-term behaviour of Dry-stacked masonry, TMS J. (2002) 9–22.
[16] H.B. Ayed, O. Limam, M. Aidi, A. Jelidi, Experimental and numerical study of Interlocking Stabilized Earth Blocks mechanical behaviour, J. Buil. Eng. 7 (2016) 207–216.
[17] M.J. Greve, C.T. Rapp, M.T. Dersch, J.R. Edwards, C.P.L. Barkan, J. Mediavilla, B. Wilson, Quantification of concrete sleeper and elastic fastening system demands utilizing concrete sleeper rail seat contact area, in: Proceedings of the World Congress on Railway Research 2013 (WCRR 2013), Sydney, Australia, (2013).
[18] S. Noor-E-Khuda, M. Dhanasekar, D.P. Thambiratnam, Out-of-plane deformation and failure of masonry walls with various forms of reinforcement, Compos. Struct. 140 (1) (2016) 262–277.
[19] M. Dhanasekar, T. Zahra, A. Jelvehpour, S. Noor-e-Khuda, D.P. Thambiratnam, Modelling of auxetic foam embedded brittle materials and structures, Appl. Mech. Mater. 846 (2016) 151–156.
[20] G. Imbalzano, P. Tran, T.D. Ngo, P.V.S. Lee, A numerical study of auxetic composite panels under blast loadings, Compos. Struct. 135 (2016) 339–352.
[21] T. Zahra, M. Dhanasekar, Characterisation of cementitious polymer mortar – auxetic foam composites, Constr. Build. Mater. 147 (2017) 143–159.
[22] I-Scan Manual, Tactile Force and Pressure Measurement System, Teckscan Inc., USA, 2013.
[23] C.S. Barbosa, P.B. Lourenco, J.B. Hanai, On the compressive strength prediction for concrete masonry prisms, Mater. Struct. 43 (3) (2010) 331–344.
[24] ABAQUS (2013). Abaqus 6.13-3 Documentation. In: (SIMULIA).
[25] R. Evans, M. Marathe, Microcracking and stress-strain curves for concrete in tension, Mater. Struct. 1 (1) (1968) 61–64.
[26] A. Bezazi, F. Scarpa, Mechanical behaviour of conventional and negative Poisson's ratio thermoplastic polyurethane foams under compressive cyclic loading, Int. J. Fatigue 29 (2007) 922–930.
[27] M.R. Sloan, J.R. Wright, K.E. Evans, The helical auxetic yarn – a novel structure for composites and textiles; geometry, manufacture and mechanical properties, Mech. Mater. 43 (2011) 476–486.
[28] D.J. White, W.A. Take, M.D. Bolton, Soil deformation measurement using particle image velocimetry (PIV) and photogrammetry, Geotechnique 53 (2003) 619–631.
[29] M.J. Greve, M.S. Dersch, J.R. Edwards, C.P.L. Barkan, H. Thompson, T.R. Sussmann, M.T. McHenry, Examination of the effect of concrete crosstie rail seat deterioration on rail seat load distribution, Transp. Res. Rec.: J. Transp. Res. Board 2476 (2015) 1–7.